Applied Ocean Research 46 (2014) 15–27

Contents lists available at ScienceDirect

Applied Ocean Research

journal homepage: www.elsevier.com/locate/apor

A wave-by-wave analysis for the evaluation of the breaking-wave celerity

Matteo Postacchini*, Maurizio Brocchini

Department of ICEA, Università Politecnica delle Marche, Ancona, Italy

ARTICLE INFO

Article history:
Received 11 April 2013
Received in revised form 28 January 2014
Accepted 30 January 2014
Available online 4 March 2014

Keywords:
Breaking waves
Celerity
Surf zone
Celerity predictors

ABSTRACT

The paper gives an overall description of the breaking-wave celerity on the basis of a wave-by-wave analysis that has been performed by using field data collected during the ECORS Project (Truc Vert Beach, France, 2008). Data coming from two pressure sensors have been analyzed with the aim to correlate, after a zero-crossing analysis, each wave of both signals. The method is based on a first correlation between 10′ time windows of both signals and, then, on the individuation of the correct time lag for each wave. Such data, which reveals a quasi-gaussian behavior of the breaking wave celerity, have also been used to relate the wave celerity with suitable wave characteristics, and comparisons are made with the most common formulas that can be found in the literature. The wave-by-wave method, validated by means of suitable laboratory test data, gives good results in the evaluation of the celerity, especially when it is made to depend on both a velocity scale and the wave non-linearity parameter. Further, a comparison with literature models used for the prediction of breaking wave celerity suggests good performances of both solitary-wave (correlation coefficient $R^2 = 0.79$) and shock-wave ($R^2 = 0.71$) theories, that give results well matched to the field data.

1. Introduction

Although the celerity of breaking waves is fundamental for the description of nearshore waves, especially in the development of both wave-averaged and wave-resolving numerical models (e.g. Boussinesq-type models), a satisfactory theory for its prediction is not available as yet. Whereas the celerity of non-breaking waves is well known, wave breaking and the related energy and momentum transformations introduce so much uncertainty in the representation of the wave flow that a complete description of wave celerity is still missing.

Only few studies on this topic are available, such as [21], that is the fundamental work that compares results of field experiments and linear-theory predictions, Tissier et al. [22] (hereinafter TI11), who analyzed field data using a cross-correlation 10′-averaged approach for the evaluation of both breaking-wave celerity and nonlinear predictors, or [8], who analyzed the video measurements performed in the nearshore region to predict the beach evolution from the breaking wave celerity. Other works, e.g. [4,7,19,20], aimed at investigating the main characteristics of breaking waves by performing laboratory experiments. Svendsen et al. [20], starting from the continuity and momentum equations and using both a constant-form wave and a constant water depth, obtained an important formula for the description of the phase speed of breaking waves, also validated by experimental tests. Such a model, known as the "classical" bore model, neglects turbulent effects and Stive [19] compares his own experimental data with Svendsen et al.'s formula [20], also taking into account turbulence, finding a good agreement. On the other hand, linear theory largely underestimates the propagation speed of surf-zone waves. More recently, Catálan and Haller [4] compared some of the most common analytical models for the prediction of the wave celerity with experimental results, obtained in a large wave flume by means of a video technique. Such a technique, also applied by Almar et al. [1], enables to recognize when a wave breaks and what is its celerity by means of images (time stacks) that are built using video recordings and represent the time evolution of the water level along a cross section of the nearshore. Further, Grue and Jensen [7] analyzed the kinematics of deep-water breaking waves in terms of local variables, like the local wave slope and the local phase speed, the latter being estimated from the nonlinear dispersion relation. They also compared their findings with the field data collected by Romero and Melville [16].

Moreover, other works that are, more generally, focused on the wave-breaking phenomenon, also investigate the celerity of breaking waves. As an example, [2] are interested in the analysis of the breaking initiation of solitary waves and, for this purpose, they compare the results of their numerical model with experimental data. They also studied the case of bore-front propagation speed overcoming a critical phase speed, that is used for the individuation of the breaking initiation. When this condition is satisfied, such a speed represents the breaking-wave celerity. Also, Okamoto

* Corresponding author. Tel.: +39 0712204539; fax: +39 0712204525.
E-mail address: m.postacchini@univpm.it (M. Postacchini).

0141-1187/$ – see front matter © 2014 Elsevier Ltd. All rights reserved.
http://dx.doi.org/10.1016/j.apor.2014.01.005

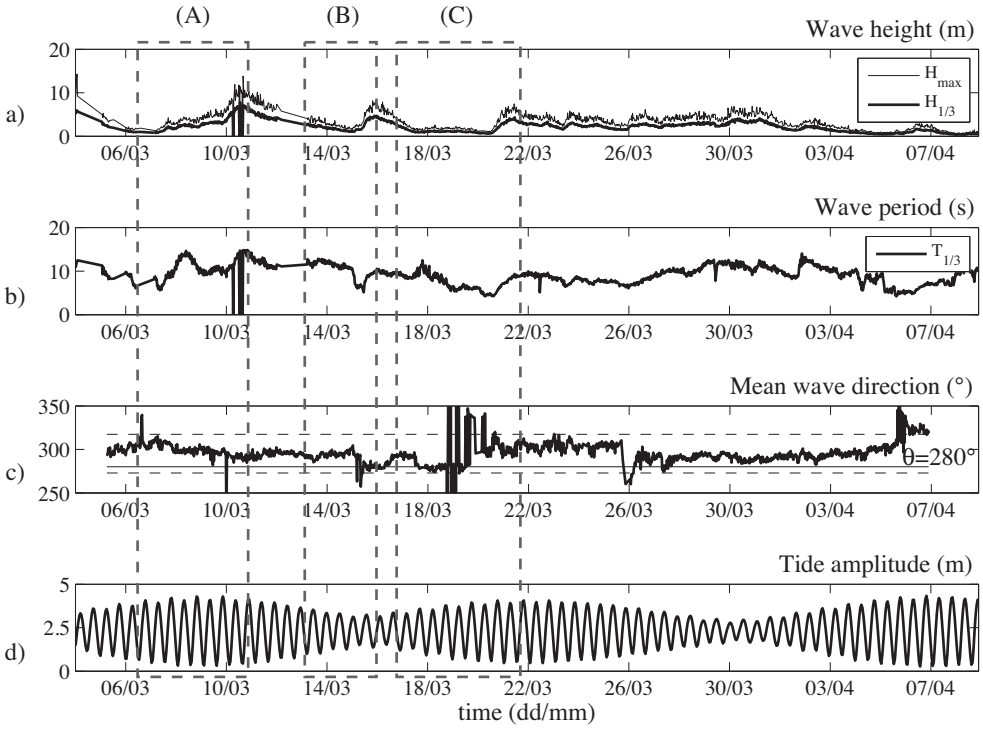

Fig. 1. Wave and tide characteristics. The three boxed areas, (A), (B) and (C), represent the recorded intervals. From top to bottom: (a) significant ($H_{1/3}$) and maximum (H_{max}) wave height; (b) significant wave period ($T_{1/3}$); (c) mean wave direction ($\theta = 280^{\circ}$ is the shore normal); (d) tide amplitude.

and Basco [13] aimed at recognizing the initiation of wave breaking using the "Relative Trough Froude Number", defined as $RTFN = (|u_{trough}| + c)/\sqrt{gd_{trough}}$, where u_{trough} is the trough velocity, c the wave celerity and d_{trough} the water depth at the trough. They correlated the particle velocity at the wave crest with the phase speed of the wave, which is the breaking-wave celerity when the former is larger than the latter. The RTFN has also been implemented in FUNWAVE, which is a numerical, depth-averaged model, based on the Boussinesq equations and developed by Kirby et al. [9].

Knowledge of the breaking-wave celerity (c_b) is particularly important for both wave-averaged and wave-resolving models. In the former models terms like mass flux, energy flux and dissipation are averaged over a wave period T, that is used, together with c_b, for the evaluation of the breaking location. On the other hand, in typical Boussinesq-type models (see, for example, [18]), that are wave-resolving, the celerity of breaking waves is parameterized using the linear, shallow water celerity ($c_{lin} = \sqrt{gh}$) and adapting it to real-life conditions through a calibration coefficient (e.g. $c_b = 1.3\sqrt{gh}$), even if this is neither the best approximation of what actually happens in the surf zone, nor a theoretically solid approach. Further, a correct prediction of the breaking wave celerity is fundamental for the application of remote sensing techniques, especially when they are used to operate a depth inversion, i.e. to reconstruct, given a sea state, the beach morphology (for more details, see [4]).

Literature studies concerning the breaking-wave celerity of real sea waves are very few, hence we dedicate the present work to this topic. The innovative approach used here is that of evaluating the breaking-wave celerity by means of a wave-by-wave analysis, that leads to the individuation of the actual celerity related to each breaking wave that is directly measured in the field. This purpose has been undertaken starting from the work of TI11, who analyzed the same field data using a 10′-averaged procedure and treating a number of waves as a group characterized by the same celerity. The novelty of our work, which we regard as complementary to that of TI11, is the analysis of each wave, that enables to find its actual celerity rather than an averaged one. In fact, TI11's approach may lead to neglect some important information about all the waves that travel and, eventually, evolve between two points that are used to estimate the breaking wave celerity. Beyond the novel procedure for the evaluation of c_b, a comparative analysis is made to assess which of the available literature formulas best represents our field data and which is the best to be used within the mentioned wave-resolving and wave-averaged models.

The paper is organized as follows. Section 2 describes the experimental set-up of the field experiments. Section 3 details the method used for the analysis of the acquired data, while Section 4 illustrates results derived from the wave-by-wave method and compares them with some analytical models. Finally, Section 5 closes the paper.

2. Experimental set-up

In a six-week period during March–April 2008 a multi-institutional campaign of nearshore field experiments was performed at the Truc Vert beach, that is about 60 km far from Bordeaux, along the southern part of the French Atlantic coast. The beach is natural, i.e. with minimal impact of human activities. The main features are those of the 100 km sandy coast located between the Gironde Estuary (on the North) and the Arcachon inlet (on the South). The morphological activity is very intense, because of both a large tide range (about 3.70 m) and high-energy wave conditions (wave heights up to 14 m in winter), and a double-barred system protects the emerged beach and limits the inshore wave height (see also TI11).

Fig. 1 shows an example of the main wave properties recorded by a wave buoy located offshore of the Truc Vert beach, in a 54 m water depth. During the experiments the significant wave height ($H_{1/3}$) ranged, in general, between 1 m and 8 m. Four storms occurred in the period of interest, including a storm characterized by a maximum wave height larger than 10 m.

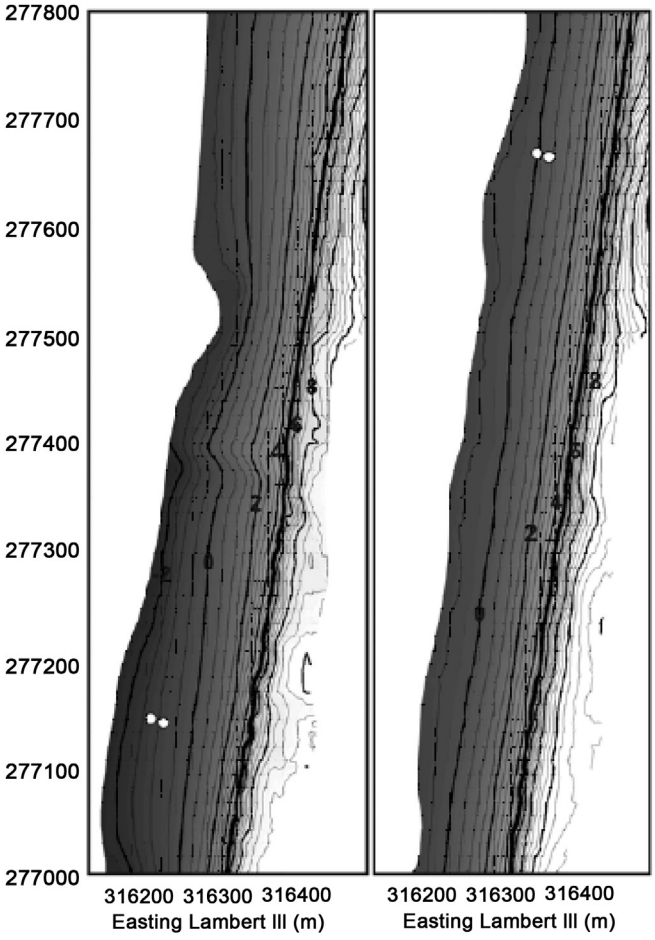

Fig. 2. Location of the pressure sensors (white circles). ADVs are deployed between the pressure sensors.
Adapted from TI11.

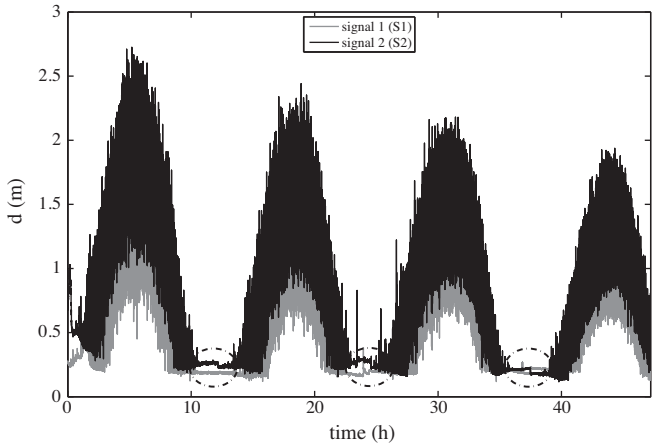

Fig. 3. Example of water depth evolution during the first tides of recording (B).

The present work focuses on the analysis of the data collected by two pressure sensors that were placed on the beach by means of vertical rods stuck into the seabed. The areas of Fig. 1, framed and labeled as A, B and C, refer to the periods in which such data were collected, each characterized by different wave and tidal conditions. The waves, reaching a maximum height $H_{max} > 10$ m in the first recording period (A), are recorded in correspondence of tides of different nature (see panel *d*) of Fig. 1), characterized by a maximum (frame A), a decreasing (frame B) and an increasing tide amplitude (frame C). Storms occurred during each of these periods.

The most inshore sensor was S1, while S2 was placed about 15 m offshore of S1 (see Fig. 2). Some recordings coming from an Acoustic Doppler Velocimeter (ADV), placed between the two pressure sensors, have also been used. All the mentioned instruments were deployed at several positions during the experiment. All of these instruments were characterized by a sampling frequency $f = 16$ Hz and were synchronized with one another.

The instruments (white points of Fig. 2 represent the pressure sensors) were placed into an intertidal zone, hence they were not under water all the time. During the low tide, measurements of the seabed were carried out, with the aim to update the vertical position of the measuring heads with respect to the evolving seabed, this being useful for the reconstruction of the water level from the pressure signals. As shown in Fig. 2, instruments were located in regions of the beach where an almost shore-parallel bathymetry was present during the field experiment. Nevertheless, as underlined by TI11, the wave refraction was not significant, hence providing a wave direction that was quasi-normal to the beach in correspondence of the instrument positions. In fact, even far offshore from the pressure sensors, i.e. at the buoy location, wave rays were close to the shore-normal direction (i.e. $\theta = 280 \pm 7^\circ$), represented by a solid line in Fig. 1, and had an incidence of $295 \pm 22^\circ$ (range represented by dashed lines), as also claimed by Sénéchal et al. [17]. Further, refraction occurring between the buoy and the pressure sensors reduced the wave incidence with respect to the shore normal, this becoming lower than 10°. Hence, it is acceptable to take the measured celerity, i.e. the cross-shore component of the celerity, as that representing the total celerity, this giving an error smaller than 2%.

Furthermore, an array of two synchronized cameras, with sampling frequency $f_v = 2$ Hz, was also used to video record the Truc Vert beach during the campaign. Video recordings were performed during the entire experiment, in the daylight. Each pair of images, captured by the cameras, generated a single plan-view image, after a rectification from pixel to world coordinates. The grid resolution in the plan-view images is $(2 \times 2)\,m^2$. It corresponds to pixel-footprint dimensions of about $(0.5 \times 1)\,m^2$, in the alongshore and cross-shore directions, respectively, at the inner-bar area, while they increase to about $(10 \times 20)\,m^2$ at the alongshore ends of the field site. More details about the video-camera deployment and the image analysis are given in [1].

3. Data analysis

From the pressure sensors the time evolution of the total water depth (d) has been obtained for all the recordings (for details, see also TI11). Fig. 3 illustrates such an evolution during the first four tides of recording (B). In the following, data of recording (B) are presented as an example of application of the procedure. Analyses and results illustrated in Section 4 are clearly valid for all recordings.

Because of the tide variation the equipment was not always submerged, hence data related to the low tides are not available (circled periods in Fig. 3 highlight the low-tide intervals). Therefore, in the following, when talking of a tide we mean the whole recorded portion of a tide; for example, the second tide of (B) refers to the data ranging between, more or less, 13 h and 23 h (see Fig. 3).

3.1. Wave-by-wave analysis

The purpose of the present paper is the individuation of the single-wave celerity. This is achieved through a precise evaluation of the wave celerity during the breaking phenomenon. The search for a good relationship between c_b and some wave features (e.g.

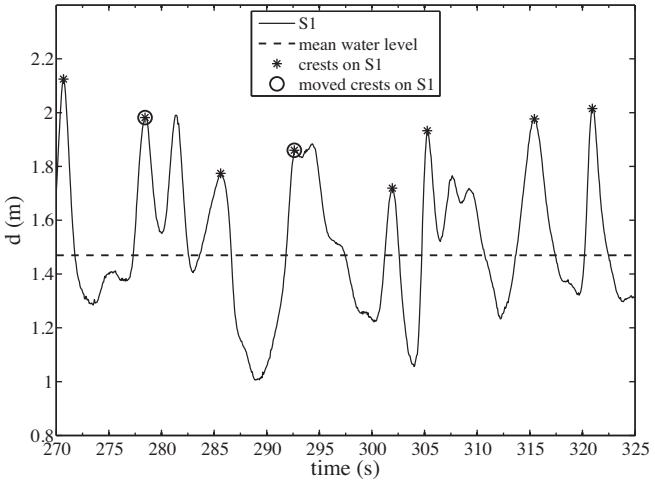

Fig. 4. Genuine wave fronts in signal S1, recorded by the first pressure transducer (black line). Asterisks are for $d_{crest} = d_{max}$ and circled asterisks for $d_{crest} \neq d_{max}$. Dashed line represents the mean water level.

non-linearity, water depth) has been also undertaken. Difficulties arise because waves largely change in shape when traveling from one pressure sensor to another and incorrect correlations between the collected signals are likely (as explained and shown in the following). At first, we performed a zero-crossing decomposition and individuated the crest position inside each wave (Section 3.1.1). Then, we found a 10′-averaged celerity around each wave through the cross-correlation technique, similarly to what described by TI11. This represents a rough estimate of the celerity of a large wave group (see Section 3.1.2). Then, such a value has been corrected through the individuation of the closest crest (see Section 3.1.3) and, with the aid of some filters for the elimination of the badly correlated waves (see Section 3.1.4), the actual wave-by-wave celerity has been found. The theoretical approach is similar to that of TI11 only for the zero-crossing decomposition, that enables one to characterize each wave with its own properties, i.e. height and period. From the subsequent step the approach changes, in fact the 10′-averaged celerity is searched by correlating one fixed frame with one moving frame (as detailed in Section 3.1.2 and shown in Fig. 5), and not two fixed frames, like in TI11, and is then corrected to find the celerity of each wave, and not a mean value like in TI11.

To test the quality of the wave-by-wave analysis, a validation has been performed using some available wave flume data (see Appendix A).

3.1.1. Wave crest individuation

The first step of the analysis consisted in a zero-down-crossing decomposition, to get the main characteristics of each wave.

Then, we found the first (in time) significant peak inside each wave, which represents the crest position, characterized by a water depth d_{crest}. For this task two thresholds have been used. The first has been used to pinpoint only local maxima higher than half of the maximum total water depth (d_{max}), previously identified with the zero-down-crossing analysis (i.e. $d_{crest} \geq 0.5 d_{max}$). The second has been used to discard those local maxima that are too close to such a maximum level and that do not represent a wave front (i.e. the time span between d_{max} and d_{crest} had to be larger than 1.2 s, that, after several calibration tests, resulted the best range to avoid inclusion of very small oscillations occurring near the local maximum).

Fig. 4 illustrates the signal S1. If the maximum depth represents a genuine wave front (i.e. $d_{max} = d_{crest}$) it is labeled by a simple asterisk (e.g. $t \cong 305$ s), otherwise ($d_{max} \neq d_{crest}$) the genuine front is identified by a circled asterisk (e.g. $t \cong 293$ s).

3.1.2. Correlation for series of 10′

A 10′ time window of data around each wave of S1 was correlated with several time frames of S2. While the window is kept fixed around the i-th wave crest of S1, a frame of 10′ moves along S2. Such a moving frame (dashed lines in Fig. 5) starts from the same time range of the fixed window (solid line) and is moved back in time (as shown by the arrows) datum by datum, to evaluate at each step the correlation coefficient with respect to the fixed series of S1. The maximum displacement of the frame is $t_{back} = 10$ s from its initial position, because it was seen that the time needed by the waves to travel from S1 to S2 is less than 10 s, thus being possible to correlate the waves in such a time span. The highest correlation coefficient was taken into account, representing the best correlation for 10′ around the i-th wave.

3.1.3. Closest crest

This step is fundamental for the correct correlation of each pair of waves.

It consists in accounting for the time span (δt^*) obtained with the cross-correlation procedure described in Section 3.1.2, which does

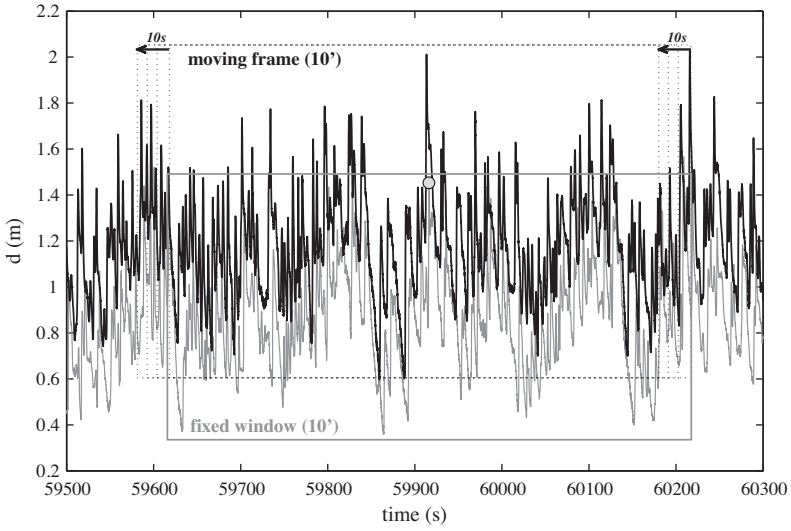

Fig. 5. Correlation between the 10′ fixed time window (solid line) around the i-th wave crest (gray dot), individuated in S1 (in gray), and the frame (dashed lines) moving along the signal S2 (in black).

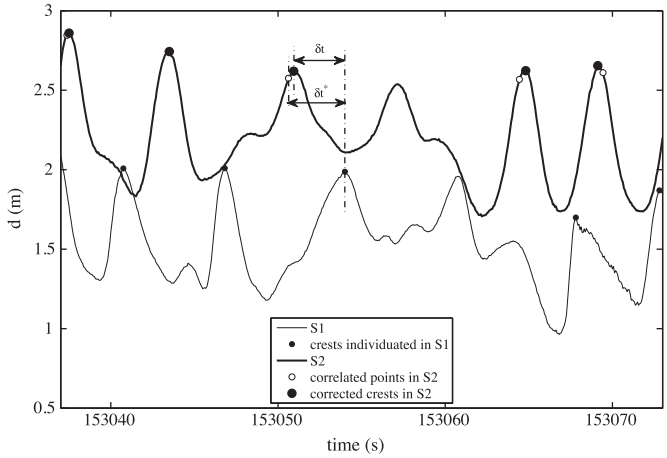

Fig. 6. Points identified in S2 (thick line) by means of a 10′ cross-correlation (white circles) and by means of cross-correlation and identification of the closest crest (large black circles). The time span between the correlated points in S2 and the crests (small black circles) in S1 (thin line) is δt^*, while δt is the lag between the S1 crests and the corrected crests. Water depth difference between S1 and S2 locations is about 65 cm.

not necessarily represent the best-correlation lag between the i-th wave of S1 and that of S2, but only the time span of best correlation between 10′ of signal S1 and 10′ of signal S2. In fact, as illustrated in Fig. 6, δt^* is the time lag between a wave crest in S1 (small black circles) and a point in S2 (white circles) that could not match with the wave crest (large black circles). Such a first-approximation point may fall before or after the real wave crest, as shown in Fig. 6. To find the real time lag (δt), the wave front of S2 (large black circles) closer to the first-approximation point is detected and the span between the i-th wave crest in S1 and the crest individuated in S2 is evaluated.

The wave celerity has been computed as:

$$c = \frac{\delta D}{\delta t}, \tag{1}$$

δD being the distance between sensors.

Fig. 7 shows an example of typical time series of wave characteristics during a recorded tide. Wave height (H) and period (T) have first been evaluated for both signals by means of the zero-down-crossing analysis and averaged, while the celerity c has been calculated as explained above.

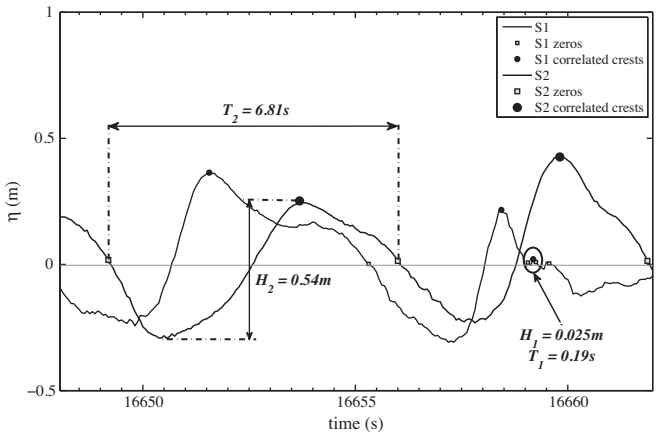

Fig. 8. Example of bad correlation of a wave between S1 and S2.

3.1.4. Data filtering

Although some thresholds had already been employed during the individuation of the wave front (see Section 3.1), other parameters had to be used to reduce errors that might be generated during both zero-down-crossing analysis and signal correlation. In the following a summary of all the employed filters is given:

(i) low-frequency elimination by means of a high-pass filter ($f > 0.05$ Hz);
(ii) elimination of waves characterized by too short periods ($T_i < 2$ s, with $i = 1, 2$);
(iii) elimination of waves characterized by very different wave periods ($T_i < 0.7T_j$, with $i, j = 1, 2$ and $i \neq j$) and heights ($H_i > 3H_j$, with $i, j = 1, 2$ and $i \neq j$).

Filter (i) is applied to the entire signals S1 and S2 to exclude infra-gravity waves. Filters (ii) and (iii) were only applied to the single waves and enable removal of both parasite waves and badly-correlated waves. The former is used to remove very high-frequency waves, e.g. small water-surface oscillations. The latter is used to disregard all the waves characterized by significantly different heights and periods, because such a difference, at times, means that the cross-correlation failed (see also Fig. 8).

Fig. 8 shows an example of possible errors: the water oscillation in S1, circled in black and with characteristics $H_1 = 0.025$ m and $T_1 = 0.19$ s, is incorrectly individuated by means of the zero-crossing

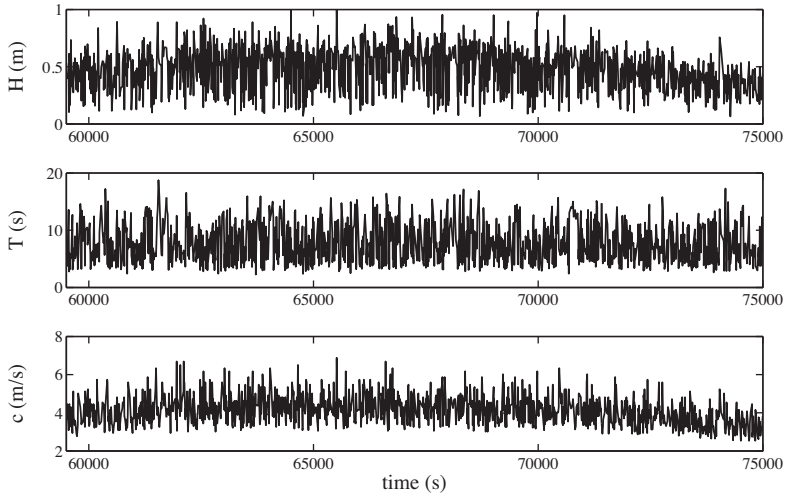

Fig. 7. Evolution in time of wave characteristics, from top to bottom, H, T and c during the second tide of recording (B).

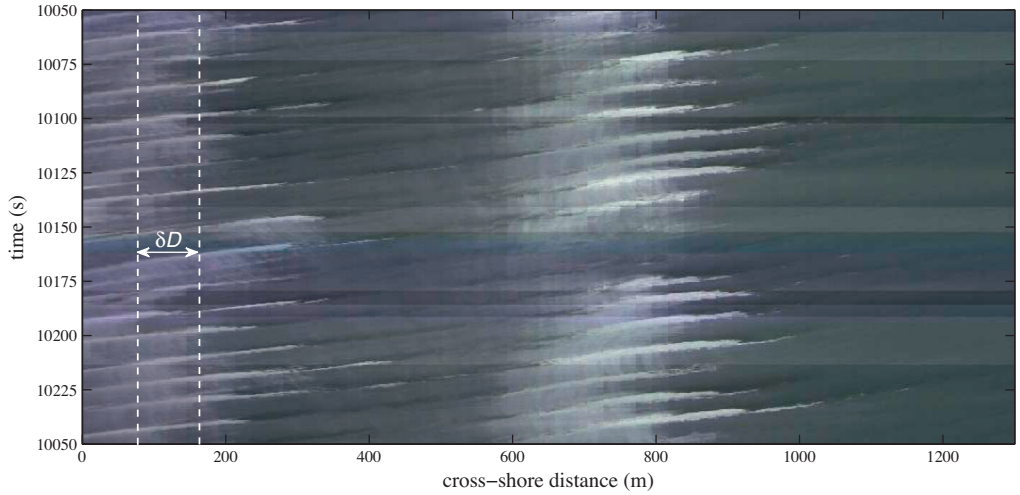

Fig. 9. Time stack: temporal data versus cross-shore distance for a portion of the fourth tide in recording (B); δD is the distance between the two pressure sensors, whose positions are represented by the white dashed lines.

procedure and, further, the wave-by-wave analysis correlates it with the wave in S2, characterized by $H_2 = 0.54$ m and $T_2 = 6.81$ s. In this special case, all the filters above-described are able to disregard such a wave correlation.

3.2. Breaking and non-breaking waves

Two different criteria have been applied to know whether a wave was breaking or not. The first method is based on the analysis of video images captured by means of an array of cameras (see Section 3.2.1). The other method evaluates the mean energy fluxes in correspondence of both pressure signals (see Section 3.2.2).

The results presented here have been obtained by using the first criterion when video recordings were available and the energy flux criterion elsewhere. A comparison of results and performances of both methods has also been made, as illustrated in Section 3.2.3.

3.2.1. Breaking waves from video images

From the video recordings, suitable images, called time stacks, have been extrapolated to represent the temporal evolution of a cross-shore section of the beach (Fig. 9).

Following [1], who describe how to deal with time stacks, we assume that the pixel intensity, derived from such images, can be linked to the water level (see also [10]). In particular the temporal evolution of two signals are analyzed in detail in each time stack, i.e. those related with the two pressure sensor positions, identified in Fig. 9 by white-dashed lines. For these deployments the pixel intensity has been evaluated to understand whether waves were breaking or not when they were passing over the sensors. After an accurate synchronization between video and pressure sensor signals the pixel color intensities have been filtered by means of a high-pass filter (0.02 Hz), to eliminate low-frequency oscillations and to have a clearer view of the intensity evolution around zero.

Fig. 10 represents signals coming from both sensors and stacks. In particular water depth (top panel) and filtered pixel intensity (bottom panel) are represented for both signals S1 (thin line) and S2 (thick line). In the top panel, circles identify the correlated wave crests for both signals while diamonds on S2 pinpoint just the breaking waves. In the bottom panel the two lines give the evolution of the intensity of the red color, that is similar to the trend of both green and blue in the RGB-scale.

In the pixel-intensity representation, the steep wave fronts appear as minima, whereas the mildly-sloping back faces are identified as maxima, because of the sun reflection on the water surface. Hence, wave crests and maximum pixel intensities are in a fairly good agreement, especially for the identification of the breaking waves. Because of a small time delay between video and pressure sensor recordings, an interval of 3 s, starting from the crest time of each pressure sensor signal, has been used to evaluate whether a local maximum was reached by the intensity signals in that time range. If so, the wave has been considered as a breaking wave.

3.2.2. Breaking waves from energy flux estimation

The second method is based on the calculation of the wave energy. For each signal the energy flux has been evaluated every 10′ of the water-level evolution. The criterion is based on the calculation of the energy flux (see also [11]):

$$F_i = E_i c_g, \quad i = 1, 2, \tag{2}$$

where E_i is the wave energy density (potential plus kinetic energy per unit area), c_g is the group velocity and subscript i refers to the pressure sensor number. They are expressed as:

$$E_i = \frac{\rho g H_{1/3}^2}{8}, \quad i = 1, 2, \tag{3}$$

$$c_g = \frac{c}{2}\left[1 + \frac{2kh}{\sinh(2kh)}\right], \tag{4}$$

where ρ is the water density, $H_{1/3}$ the significant wave height, c the wave celerity, k the wave number ($k = 2\pi/L$, L as the wave length) and h the still water level.

The breaking waves have been chosen as those characterized by a sensible energy decay, i.e. such that the energy flux was larger at the offshore sensor (S2) than at the inshore sensor (S1), i.e. $F_2 > F_1$, as illustrated in Fig. 11.

3.2.3. Comparison between criteria for breaking estimation

The application of the criteria described in Sections 3.2.1 and 3.2.2 leads to results that, sometimes, differ. In fact, the energy flux criterion, based on the evaluation of the energy owned by all the waves that are included in a 10′-long time series, is clearly a rough method to decide whether a single wave is breaking or not, while the video criterion is based on the brightness of each wave crest and can lead to a more detailed analysis.

Fig. 12 illustrates the breaking waves individuated by means of the energy flux (squares) and the video image method (diamonds). The comparison suggests how the rougher energy flux criterion

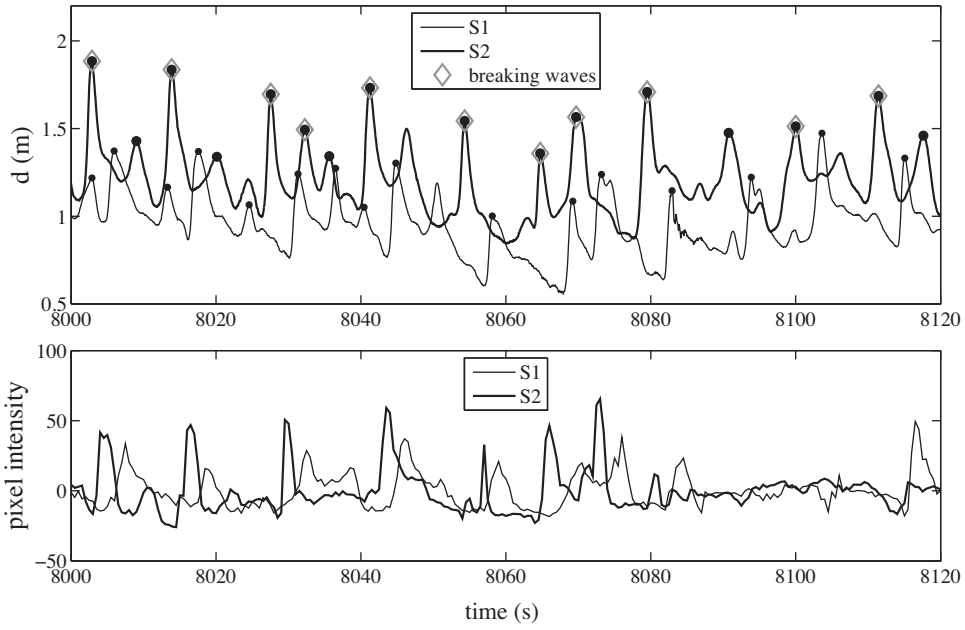

Fig. 10. Example of derivation of water depth from the pressure sensors (top panel) and pixel intensity for the positions S1 and S2 (bottom panel) for a portion of recording (B).

labels waves as "breaking" with a higher (30%) occurrence than the more accurate method based on video images.

3.3. Velocity measurements

Comparison of the results obtained from the wave-by-wave analysis with breaking wave celerities evaluated from the literature also requires knowledge of the trough velocity of each wave (see the original shock wave theory (11) in Section 4.3). Hence, the use of an ADV to measure such a flow velocity was needed. The ADV, recording the 3 spatial components of the velocity vector at a point, was placed about 40 cm over the sea bottom, in the middle of the pressure sensor alignment and synchronized with both sensors.

Since the ADV works with acoustic signals, the signal itself is sometimes noisy, especially when the probe is not perfectly submerged. Hence, the signal has been low-pass filtered (frequency equal to 0.5 Hz). To improve the level of confidence of the resulting velocities, all waves characterized by very high or very low trough velocities (i.e. $|u_1| > 2$ m/s) were not taken into account.

Given that δt is the time lag for a wave to travel from S1 to S2, $\delta t/2$ is, approximately, the time to move from S1 to the ADV position (see Fig. 13). Hence, the minimum cross-shore velocity of a given wave must be sought over a time span of about $\delta t/2$ from the wave trough identified in S1. For this reason and to be sure to find the correct trough velocity, a time range equal to δt has been used to search for the minimum velocity in the ADV signal.

The minimum velocity of each wave can be considered as the mean horizontal velocity under the wave trough. In fact, in shallow waters the horizontal particle velocity is almost constant over the vertical, even if waves are breaking (see, for example, [12]). In the present case, from the analysis of the frequency dispersion parameter $\mu = h/L$, the majority of the waves (about 70%) is found to be in shallow water condition. Hence, the measured velocity is very

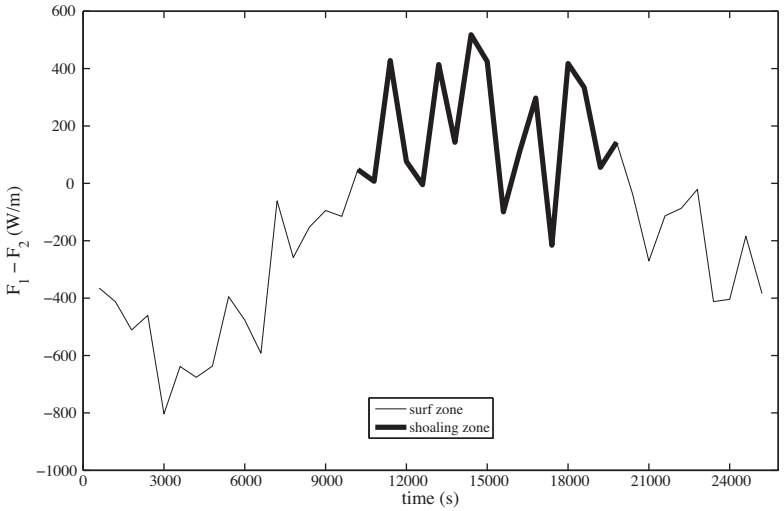

Fig. 11. Example of the temporal evolution of the energy flux difference between the onshore (F_1) and the offshore sensor (F_2). *Surf zone* data are given by a thin line, while those of the *shoaling zone* by a thick line.

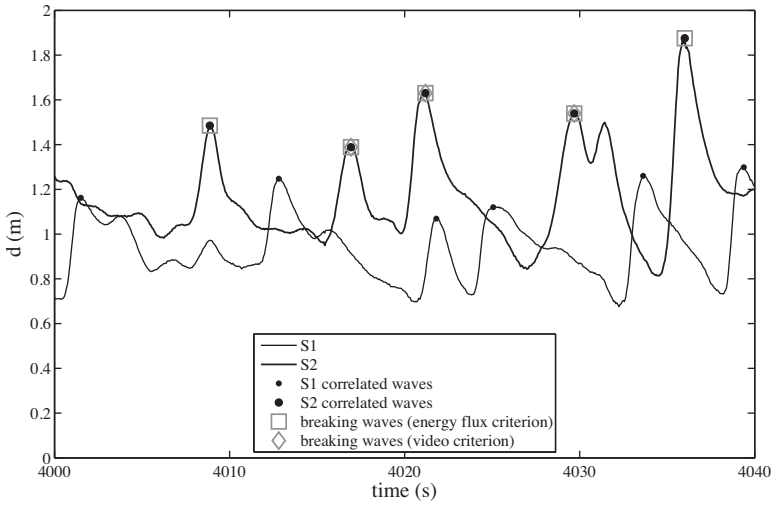

Fig. 12. Example of comparison between the energy flux method (squares) and the video criterion (diamonds) for the individuation of breaking waves in recording (B).

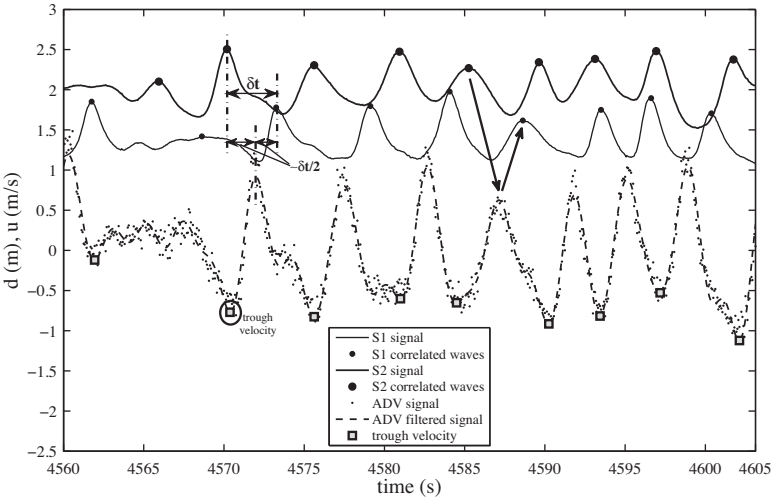

Fig. 13. Example of signals from pressure sensors (solid lines) and ADV (dots and dashed line for original and filtered signal, respectively) of recording (B).

close to the mean horizontal velocity under the wave trough (u_1), where no significant variations occur, as also shown by Cox et al. [5] in their experiments and numerical simulations.

In Fig. 13 signals from the pressure sensors are represented by thin (S1) and thick (S2) lines, while the ADV data are given in terms of both original (dots) and filtered (dashed line) signals. Crests in the water-depth signals are correlated crests if they are labeled by dots. Squares in the filtered ADV signal are minimum velocities. Arrows show the temporal displacement of a wave crest from one probe to another one (S2 crest → ADV crest → S1 crest), while the black circle identifies the trough velocity associated with the wave that is characterized by a time lag δt between S1 and S2.

4. Results

The analyses performed on the ECORS data have led to useful results concerning the behavior of breaking waves approaching the shore over a dissipative beach. Fig. 14 illustrates the gaussian probability density function (pdf, black line) and the normalized relative frequency (bins) of the analyzed c_b. This suggests a quasi-gaussian behavior of c_b, which is characterized by an average $\overline{c}_b = 4.4695$ m/s, a standard deviation $\sigma_c = 1.0898$ m/s, a skewness $s_c = 0.9363$ m/s ($\cong 0.2\overline{c}_b$) and a kurtosis $k_c = 4.7427$ m/s ($\cong 3.4\sigma_c^4$).

In the following, we show how breaking-wave celerities are related to other wave characteristics, like the wave non-linearity parameter $\epsilon = H/h$. Such relationships are searched both in the whole recorded tides and in small portions of the data set, i.e. those

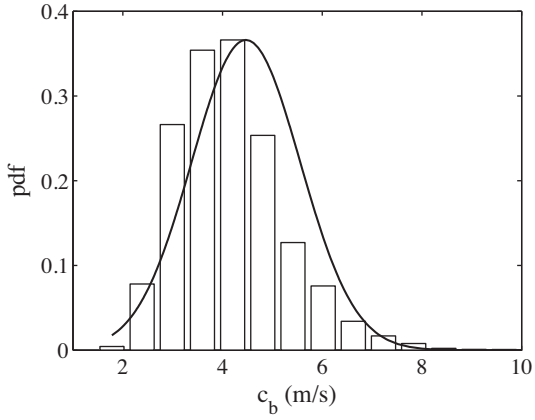

Fig. 14. Probability density function (black line) and normalized relative frequency (bins) of the analyzed breaking wave celerities.

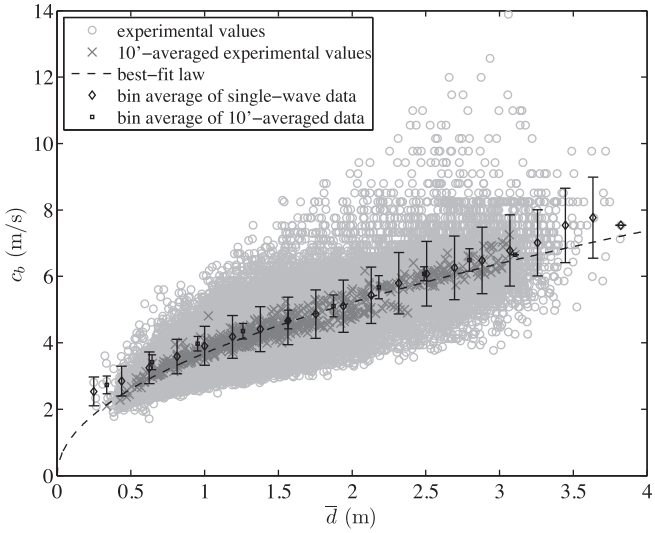

Fig. 15. Breaking wave celerity c_b of single waves (light gray circles) and averaged over 10′ (dark gray crosses) versus mean water level $\overline{d}$. The dashed line represents the best fit for the single-wave data ($c_b = 1.18\sqrt{g\overline{d}}$). Bin averages and error bars are also represented.

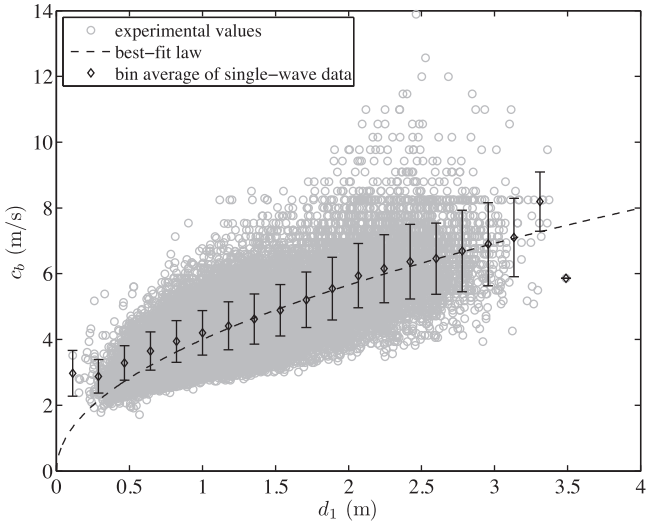

Fig. 16. Breaking wave celerity c_b of single waves versus trough-level water depth d_1. The dashed line gives the best-fit law $c_b = 1.28\sqrt{gd_1}$. Bin averages and error bars are also represented.

referring to the highest part of each tide. Some comparisons with analytical models are also performed.

4.1. Breaking wave celerity versus water depth

The celerity of breaking waves obtained from the pressure sensor data is seen to correlate well with parameters like the mean total water depth $\overline{d}$ (evaluated as the period-averaged total water depth).

The dependence on $\overline{d}$ of the celerity of single breaking waves (light gray circles) and of mean celerities averaged over 10′ (dark gray crosses) is illustrated in Fig. 15. Black symbols and error bars represent, respectively, bin averages and standard deviations of both datasets. The single-wave data are characterized by a standard deviation $\sigma = 1.10$, the 10′-averaged data by $\sigma = 0.94$. The dashed line is the best fit of the single-wave data (the standard error is $RMSE = 0.70$):

$$c_b = 1.18\sqrt{g\overline{d}}. \tag{5}$$

Such a prediction partially agrees with Dimas and Dimakopoulos's model [6], that uses 1.2 instead of 1.18 in Eq. (5), this varying in the range [1.176, 1.179].

Such a dependence is almost the same found for the 10′-averaged celerities by TI11, who found $c_b = 1.14\sqrt{g\overline{d}}$. In fact, it is simple to see how the gray crosses of Fig. 15 are well represented by the best-fit line, that is similar to that obtained by TI11. Hence, despite the difference in the method applied here and in TI11 for the evaluation of 10′-averaged celerities, the results are almost the same, suggesting validity and robustness of the present, more accurate, method.

The relationship between breaking-wave celerity and trough-level water depth (d_1) is as good as the previous one, with the same standard deviation $\sigma = 1.10$. The best-fit law is illustrated in Fig. 16 by the dashed line and its formulation is (the standard error is $RMSE = 0.76$):

$$c_b = 1.28\sqrt{gd_1}. \tag{6}$$

The multiplying coefficient varies in the range [1.274, 1.279].

4.2. Breaking wave celerity versus wave non-linearity

Relationships (5) and (6) give proportionality between c_b and depth-dependent velocity scales (i.e. $\sqrt{g\overline{d}}$ and $\sqrt{gd_1}$) in terms of a constant (i.e. 1.18 and 1.28). We now try to refine such a dependence in such a way to account for wave non-linearity. In other words, we attempt at replacing (5) with:

$$c_b = f(\epsilon)\sqrt{g\overline{d}}, \quad with \quad \epsilon = \frac{H}{\overline{d}}. \tag{7}$$

The relationship between c_b and ϵ is not as clear as expected. In fact, a large data dispersion is observed when single waves are plotted together, thus giving a very large range of ϵ for the same celerity. On the other hand, 10′-averaged values are grouped around the best-fit line, as shown in Fig. 15 for c_b and $\overline{d}$. This aspect also confirms that when a 10′ correlation is performed (TI11's approach), some useful information is disregarded. In fact, we here demonstrate that a wave-by-wave analysis is fundamental to understand the range of application of empirical laws like (7).

Hence, to find a good relationship between c_b and ϵ in the case of single waves, a reduced set of data has been used, i.e. only those referring to a portion of the high tide (e.g., the time span (18–20) h in Fig. 3) of each recording. In fact, in such conditions the hydrodynamic behavior of waves may be taken as constant, being the still water level almost constant and the tidal oscillation almost null. Such a data reduction enables us to disregard the tide variation, that is clearly a fundamental parameter that influences the correlation between breaking-wave celerity and non-linearity parameter. For such a purpose, for each recorded tide only half hour of waves around the tide peak has been taken into account.

Such high-tide celerities, plotted in Fig. 17 versus ϵ, can be compared with TI11's results. Celerities of single waves (circles) refer to half-hour waves around the tide peaks while mean celerities averaged over 10′ (crosses) refer to the entire duration of each tide. Both data have been made dimensionless by means of the celerity ($c = \sqrt{g\overline{d}}$). Black diamonds and squares plus error bars represent, respectively, bin averages and standard deviations of both datasets. The solid line represents the law found by TI11:

$$\frac{c_{TI11}}{\sqrt{g\overline{d}}} = 1.3\epsilon^2 - 0.23\epsilon + 1, \tag{8}$$

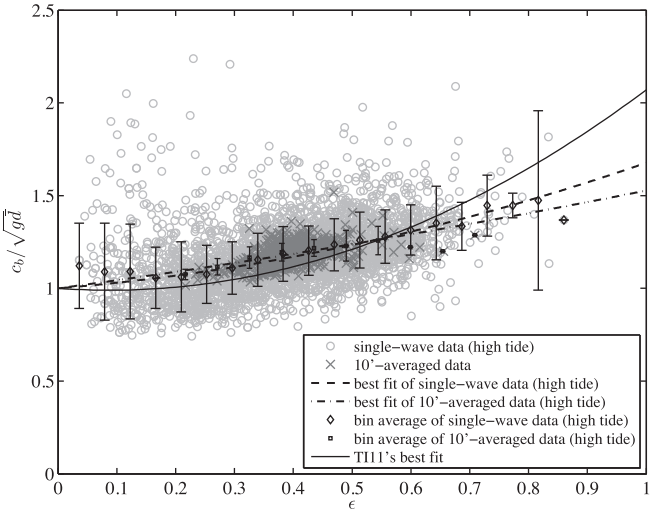

Fig. 17. Dimensionless celerity versus non-linearity parameter (ϵ). Light gray circles represent single waves and dark gray crosses 10′-averaged values. Best fits of both wave-by-wave data (dashed line) and 10′-averaged data (dash-dotted line), together with TI11's law (solid line), bin averages and error bars are also reported.

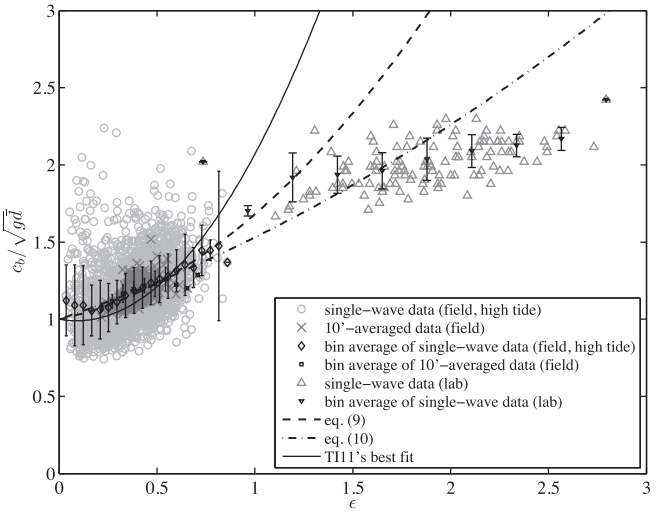

Fig. 18. Dimensionless celerity versus non-linearity parameter (ϵ). Single-wave data and bin averages of both the ECORS Project field experiment (circles and diamonds) and the laboratory experiment described in Appendix A (upward and downward triangles) are illustrated. Eqs. (9), (10) and TI11's law are also reported.

that is the best relationship between breaking wave celerity averaged over 10′ and ϵ (note that (8) is the correct formula, while in TI11 a wrong coefficient, multiplying ϵ^2, appears). The dashed black line is the best-fit law for the wave-by-wave data during the high tide (the standard error is *RMSE* = 0.16):

$$\frac{c_{b,wbw}}{\sqrt{g\bar{d}}} = 0.42\epsilon^2 + 0.26\epsilon + 1, \tag{9}$$

while the dash-dotted line is the best-fit law for the 10′-averaged experimental data (the standard error is *RMSE* = 0.05):

$$\frac{c_{b,10'}}{\sqrt{g\bar{d}}} = 0.10\epsilon^2 + 0.43\epsilon + 1. \tag{10}$$

The multiplying coefficients of (9) vary in the ranges [0.31, 0.53] and [0.20, 0.31], those of (10) in the ranges [−0.06, 0.26] and [0.36, 0.49]. Although the black data are, obviously, more scattered than the gray data, its best fit is not far from that of the gray data and that of TI11.

In summary, despite what claimed by TI11, a clear dependence of the breaking wave celerity on the wave non-linearity parameter ϵ can be obtained only if high-tide data are taken into account. The validity of the best-fit laws is better demonstrated by means of Fig. 18, where the data of Fig. 17 are plotted together with the single-wave data obtained from the laboratory experiment described in Appendix A. The latter values are characterized by a larger non-linearity parameter ϵ, with respect to the small non-linearity data of the field experiment, and are fairly well described by Eq. (10).

4.3. Shock theory validation

As already said, water velocities have been acquired by means of an ADV, that was placed in the middle of the alignment S1–S2, and have been used for the application of the "shock" theory. The original formulation of such a theory comes from Saint Venant's shock-wave solution, which provides an estimate of the breaking

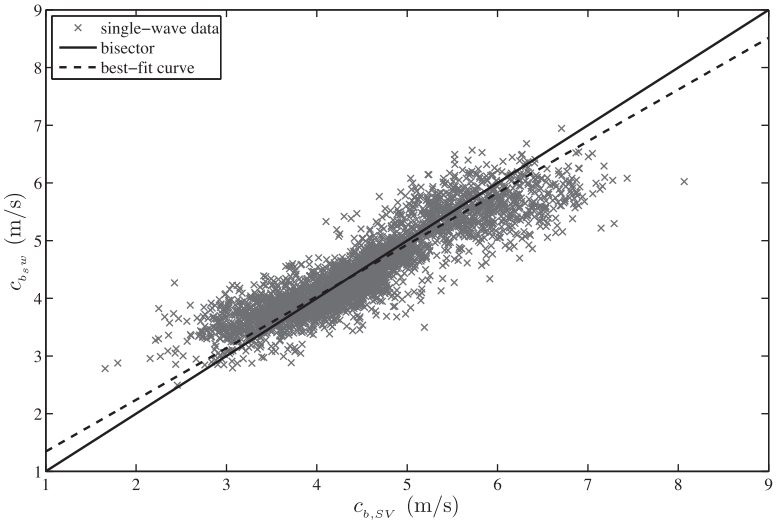

Fig. 19. Bonneton's [3] breaking wave celerity (12) versus original shock theory (11) during high tide conditions, for all the recorded series. Solid and dashed lines represent, respectively, the bisector and the data best fit.

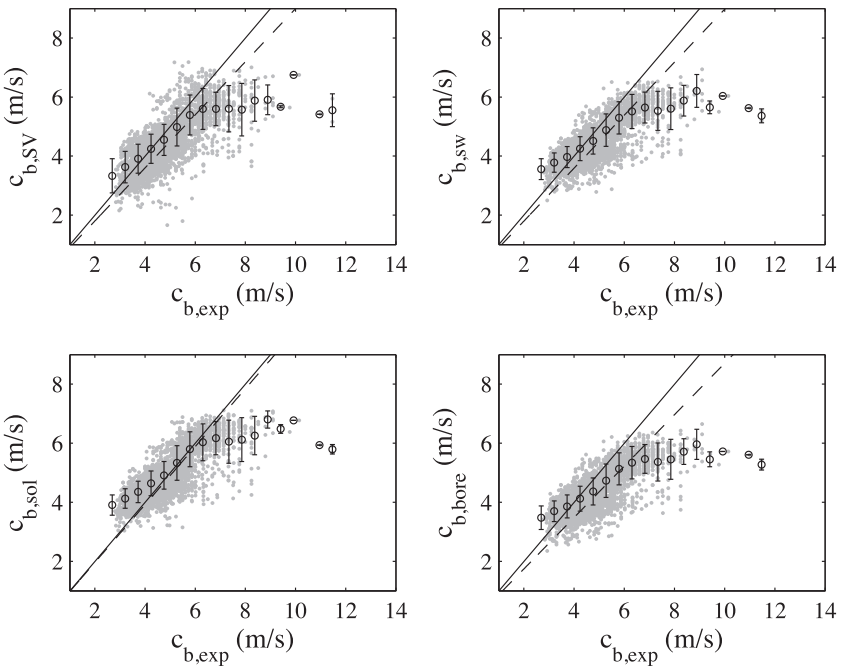

Fig. 20. Comparison between theoretical and experimental celerities computed for high tide conditions. The top-left panel refers to (11), the top-right panel to (12), the bottom-left panel to (14) and the bottom-right panel to (15). Gray circles refer to the single wave, solid and dashed lines represents, respectively, the bisector and the data best fit; bin averages and error bars are also shown.

wave celerity in terms of the trough level d_1, the crest level d_2 and the trough velocity u_1:

$$c_{b,SV} = u_1 + \left[\frac{gd_2}{2d_1}(d_2 + d_1)\right]^{1/2}. \tag{11}$$

Bonneton [3] provides a simplified version of such a shock-wave celerity which does not require knowledge of u_1, but only requires knowledge of water levels:

$$c_{b,sw} = -2(g\bar{d})^{1/2} + 2(gd_1)^{1/2} + \left[\frac{gd_2}{2d_1}(d_2 + d_1)\right]^{1/2}. \tag{12}$$

As already clarified in Section 4.2, only the experimental data collected during the maximum tidal range have been considered to evaluate both theoretical formulas. Their relationship is described in Fig. 19, which shows that (12) approximates well (11). In fact, the best-fit law (dashed line) of the experimental data is:

$$c_{b,sw} = 0.90c_{b,SV} + 0.45, \tag{13}$$

that is close to the bisector, while the correlation coefficient between experimental and theoretical data is $R^2 = 0.91$.

4.4. Comparison with analytical models

By using the data referring to the high-tide data it is also possible to inspect the performances of classical wave theories in describing the experimental data. In particular four theories have been analyzed here and plotted in Fig. 20. The top panels show, respectively, the comparison of the experimental data with the above-described "shock" theories, i.e. (11) (top-left) and (12) (top-right).

The third theory is the "solitary wave" theory, for which c_b depends directly on ϵ, compared with the experimental celerity in the bottom-left panel of Fig. 20:

$$c_{b,sol} = \sqrt{g\bar{d}(1+\epsilon)}. \tag{14}$$

The "bore" theory, illustrated in the bottom-right panel of the same figure, was proposed by Svendsen et al. [20]:

$$c_{b,bore} = \sqrt{\frac{gd_1d_2(d_1+d_2)}{2\bar{d}^2}}. \tag{15}$$

Each panel of Fig. 20 is characterized by the wave-by-wave data (gray circles). The solid line gives the bisector, that represents the perfect overlapping of experimental and theoretical data. The dashed line is the best fit of the wave-by-wave data. Further, empty circles and error bars represent, respectively, bin averages and standard deviations. Inspection of Fig. 20 suggests that the solitary-wave theory gives the best correlation, because both lines are very close, the dashed line being described by the law:

$$c_{b,sol} = 0.98c_{b,\mathrm{exp}}, \tag{16}$$

which is very close to the bisector. Further, the correlation coefficient between data and bisector is $R^2_{sol} = 0.79$, while, for the other theories, such a coefficient is lower: $R^2_{bore} = 0.64$ for the bore theory, $R^2_{sw} = 0.71$ for Bonneton's [3] shock theory and $R^2_{SV} = 0.68$ for Saint Venant's shock-wave solution.

Hence, despite the simplicity of the solitary wave theory, this leads to the best approximation of the breaking wave celerity obtained from the available field data. As claimed by TI11, the bore model of Svendsen et al. [20] gives the worst results, largely underestimating the phase speed in the surf zone. Both top panels of Fig. 20 show a fairly good adaptation of the shock-wave theories to the experimental data, especially for Bonneton's law [3] (12), despite the prediction is not as good as that given by the solitary wave theory. A possible explanation of the non-optimal performances of the original shock-wave theory (11) is the use of the particle velocity, measured under the wave trough, as the representative velocity of the entire water column. It leads to very scattered data, especially in the presence of short waves, that cannot be taken to evolve in shallow-water conditions.

In summary, use of the solitary wave theory (14), that accounts for the non-linearity parameter ϵ, leads to good results in the prediction of the breaking wave celerity, while other, even more

complicated, formulations provide worse results. However, Fig. 20 reveals that saturation is such that the growth of the experimental celerities cannot be matched by the analytical predictive laws.

5. Conclusions

A new method for the evaluation of the breaking wave celerity has been illustrated. The method is based on a wave-by-wave analysis of field data, collected during the ECORS-Truc Vert 2008 experimental campaign, by using two pressure sensors. The difficulty in the correlation of each pair of waves recorded by the sensors has been tackled through an initial cross-correlation between 10′-long time series of each instrument and a consequent wave-by-wave correction to find the time-lag between each pair of crests. The celerity has been calculated as the ratio between the sensor distance, which was constant during the data acquisition, and the time-lag.

Once the celerity has been found and all the possible errors due to both cross-correlation and zero-crossing analysis eliminated, breaking waves have been individuated by means of both a video and an energy-flux criterion, the former giving more accurate results. The method has been validated on the basis of available wave flume data. The validation has demonstrated that the method performs very well for the evaluation of random wave celerity, this testifying on the reliability and quality of the chosen approach.

The breaking wave celerity calculated for the ECORS field experiments shows a quasi-gaussian distribution. When all the wave-by-wave data of the breaking-wave celerity c_b are made to depend on the water depth, i.e. both period-averaged and trough water depths, they are seen to adapt well to the velocity scale ($\sqrt{gd}$ and $\sqrt{gd_1}$, respectively), despite some dispersion. On the other hand, if more accurate relationships are sought and c_b is related to the non-linearity parameter ϵ, the experimental-data distribution is very spread if the whole tidal cycle is taken into account, whereas clearer relationships are found if wave-by-wave data characterizing small portions of the data set, i.e. those referring to the high tide, when the influence of the tidal oscillations can be neglected, are analyzed. This clearly underlines the lack of information of an averaged method of analysis, like that of TI11, that leads to less accurate breaking-wave-celerity laws and to their improper use. Then, the comparison with literature models confirms that the solitary-wave theory provides a good correlation with the experimental celerities ($R^2 = 0.79$), while Bonneton's relationship [3], based on the shock-wave theory, gives a slightly poorer ($R^2 = 0.71$), still good, adaptation.

In summary, the breaking-wave celerity can be represented as either proportional to only a velocity scale, similar to the non-linear shallow water celerity, or also dependent on the wave non-linearity. In the latter case, a good formulation of c_b can be found if only the high-tide celerities are used.

Acknowledgements

Thanks go to Prof. Philippe Bonneton, Dr. Rafael Almar and Dr. Marion Tissier for their contribution to the drafting of an early version of the present manuscript. Special thanks go to Prof. Philippe Bonneton and Dr. Rafael Almar for granting use of the data described in the present work. The authors also thank Prof. J.P. Parisot for GPS positioning and topography and Dr. P. Bretel for the instrument deployment. All the financial support of the field experiment in the framework of the ECORS project, in particular the SHOM-DGA, is acknowledged. The authors acknowledge the partial financial support by: (1) the Italian RITMARE Flagship Project, a National Research Programme funded by the Italian Ministry of University and Research, (2) the EC FP7 Marie Curie Actions People, Contract PIRSES-GA-2011-295162 ENVICOP project (Environmentally Friendly Coastal Protection in a Changing Climate), (3) the US-ONR, through the NICOP Research Grant (N62909-13-1-N020).

Appendix A. Validation with flume experiments

We validate the technique described in Section 3 with some experimental results on wave breaking over submerged breakwaters.

The experiments were performed at the Hydraulics Laboratory of the "Università Politecnica delle Marche", where a wave flume is used for maritime models in reduced scale. The flume is 50 m long, 1 m wide and 1.3 m high and was equipped with electro-sensitive wave gauges used water-levels measurements. A typical cross-shore section of the Italian East coast beaches was reproduced in the flume. The used geometric scale was 1:20, while hydrodynamic forces and sediments were reproduced using, respectively, the Froude similitude and the Dean analogy (for more details, see [14,15]).

We here use a wave train that reproduces a JONSWAP-type spectrum characterized by a significant height $H_s = 0.09$ m and a peak period $T_p = 1.92$ s. The time series of the free-surface level η were collected by two wave gauges placed inshore (IG) and offshore (OG) of a submerged breakwater. The majority of the waves broke over the structure.

The wave-by-wave analysis has been applied to such a laboratory case, with the aim to check the validity of the described technique in a controlled environment. For the reduced scale of the laboratory tests, the moving and fixed frames described in Section 3.1.2 have been changed in 1′ time windows. Further, because of the very small wave periods of the reproduced random waves, the filter (ii) described in Section 3.1.4 has not been used.

Fig. 21 shows a portion of the time series used for the wave-by-wave analysis: the thin line represents the IG signal, the thick line represents the OG signal, while an asterisk is used for each wave crest and a circle for the only correlated crests.

Fig. 22 illustrates the wave characteristics obtained using the zero-down-crossing decomposition (H and T, top and bottom panels, respectively) and the entire wave-by-wave analysis (c, bottom panel).

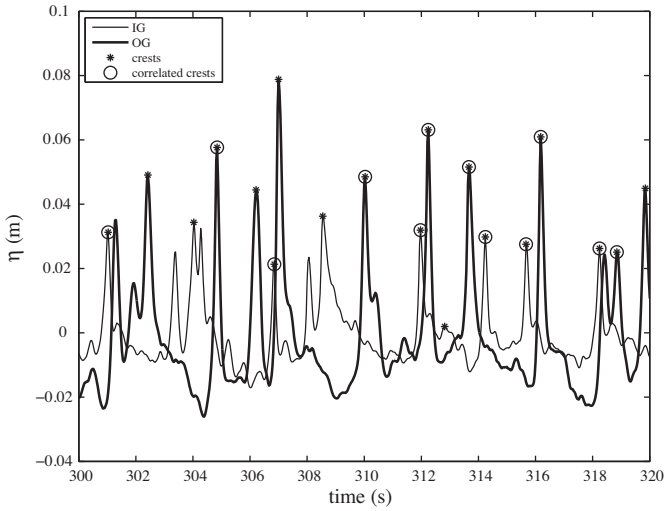

Fig. 21. Correlation between signals of inshore (IG) and offshore (OG) wave gauges.

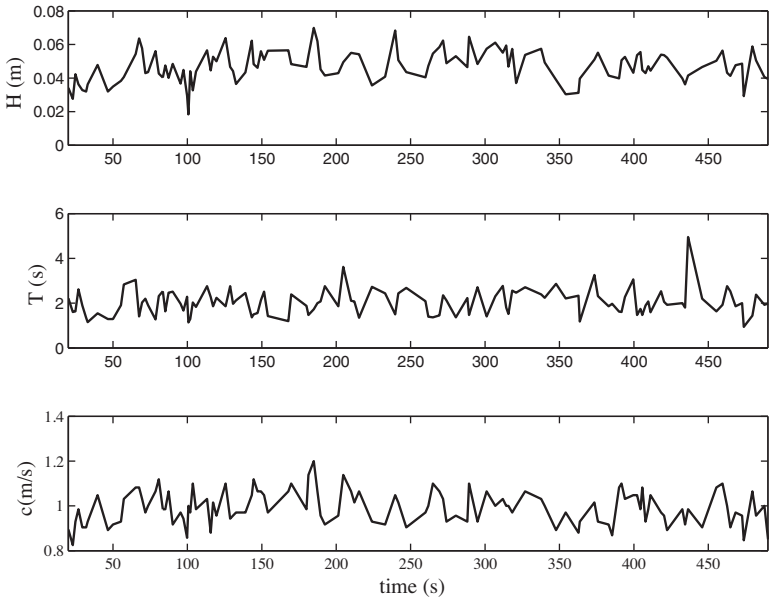

Fig. 22. Evolution in time of wave characteristics, from top to bottom, H, T and c for the flume experiments.

References

[1] Almar R, Castelle B, Ruessink BG, Sénéchal N, Bonneton P, Marieu V. Two- and three-dimensional double-sandbar system behaviour under intense wave forcing and a meso-macro tidal range. Cont Shelf Res 2010;30:781–92.

[2] Bjørkavåg M, Kalisch H. Wave breaking in Boussinesq models for undular bores. Phys Lett A 2011;375:1570–8.

[3] Bonneton P. Wave celerity in the inner surf zone. In: Proc. 29th int. conf. on coast. eng., ASCE. 2004. p. 392–401.

[4] Catálan PA, Haller MC. Remote sensing of breaking wave phase speeds with application to non-linear depth inversion. Coast Eng 2008;55:93–111.

[5] Cox DT, Kobayashi N, Okayasu A. Vertical variations of fluid velocities and shear stress in surf zones. In: Proc. 24th int. conf. on coast. eng., ASCE. 2004. p. 98–112.

[6] Dimas AA, Dimakopoulos AS. Surface roller model for the numerical simulation of spilling wave breaking over constant slope beach. J Waterw Port Coast Oc Eng 2009;135(5):235–44.

[7] Grue J, Jensen A. Orbital velocity and breaking in steep random gravity waves. J Geophys Res 2012;117:C07013, doi:10.1029/2012JC008024.

[8] Holman RA, Holland KT, Lalejini DM, Spansel SD. Surf zone characterization from unmanned aerial vehicle imagery. Ocean Dyn 2011;61:1927–35.

[9] Kirby JT, Wei G, Chen Q, Kennedy AB, Dalrymple RA. FUNWAVE 1.0 Fully Nonlinear Boussinesq Wave Model Documentation and User's Manual. Research Report No. CACR-98-06, Center for applied coastal research. Newark, Delaware: University of Delaware; 1998.

[10] Lippmann TC, Holman RA. Phase speed and angle of breaking waves measured with video techniques. In: Proc. coastal sediments '91 – ASCE. 1991. p. 542–56.

[11] Lisi I, Molfetta MG, Bruno MF, Di Risio M, Damiani L. Morphodynamic classification of sandy beaches in enclosed basins: the case study of Alimini (Italy). J Coast Res, SI 2011;64:180–4.

[12] Mei CC. Applied dynamics of ocean surface waves. New York: John Wiley & Sons; 1983.

[13] Okamoto T, Basco DR. The relative trough froude number for initiation of wave breaking: theory, experiments and numerical model confirmation. Coast Eng 2006;53:675–90.

[14] Postacchini M, Brocchini M, Corvaro S, Lorenzoni C, Mancinelli A. Comparative analysis of sea wave dissipation induced by three flow mechanisms. J Hydraul Res 2011;49(4):554–61.

[15] Postacchini M, Brocchini M, Mancinelli A, Landon M. A multi-purpose, intra-wave, shallow water hydro-morphodynamic solver. Adv Water Resour 2012;38:13–26.

[16] Romero L, Melville WK. Spatial statistics of the sea surface in fetch-limited conditions. J Phys Oceanogr 2011;41:1821–41.

[17] Sénéchal N, Abadie S, Gallagher E, MacMahan J, Masselink G, Michallet H, et al. The ECORS-Truc Vert08 nearshore field experiment: presentation of a three-dimensional morphologic system in a macro-tidal environment during consecutive extreme storm conditions. Ocean Dyn 2011;61:2073–98.

[18] Schäffer HA, Madsen PA, Deigaard RA. A Boussinesq model for waves breaking in shallow waters. Coast Eng 1993;20:185–202.

[19] Stive MJF. Energy dissipation in waves breaking on gentle slopes. Coast Eng 1984;8:99–127.

[20] Svendsen I, Madsen P, Hansen J. Wave characteristics in the surf zone. In: Proc. 16th int. conf. on coast. eng., ASCE. 1978. p. 520–39.

[21] Thornton EB, Guza RT. Energy saturation and phase speeds measured on a natural beach. J Geophys Res 1982;87(C12):9499–508.

[22] Tissier M, Bonneton P, Almar R, Castelle B, Bonneton N, Nahon A. Field measurements and non-linear prediction of wave celerity in the surf zone. Eur J Mech B/Fluids 2011;30:635–41.